Journal of Magnetic Resonance **144,** 288–296 (2000)
doi:10.1006/jmre.2000.2050, available online at http://www.idealibrary.com on IDEAL®

Magnetic Resonance Imaging of Electroconvection in a Polar Organic Solvent

Scott A. Riley and Matthew P. Augustine[1]

Department of Chemistry, One Shields Avenue, University of California, Davis, California 95616

Received October 20, 1999; revised February 2, 2000

Molecular motion in the polar organic solvent nitrobenzene induced by an electric field is studied by magnetic resonance imaging. Rf pulse sequences that correlate images obtained at two different times under conditions of both continuous and pulsed electric fields are introduced. The resultant image correlation spectra indicate that the time scale of motion in a 9.6 kV/cm electric field is tens of milliseconds. Comparison of the results to an analytic solution for the Fokker–Planck probability function for one-dimensional bounded diffusion yields an electric field dependent effective diffusion coefficient for perdeuterated nitrobenzene of $D = 1.08 \times 10^{-5}$ cm^2/s + $(3.33 \times 10^{-3}$ cm^4/kV^{2}s$)$ E^2 at room temperature. Characteristics of this electroconvection and its consequences for combining multidimensional nuclear magnetic resonance with electrical orientation are also discussed.

Key Words: **diffusion; electric field alignment; electroconvection; magnetic resonance imaging; molecular motion.**

INTRODUCTION

Determination of chemical structure and biological function is central to the field of nuclear magnetic resonance (NMR) spectroscopy (*1–3*). As is well established in the study of liquid samples with NMR, one typically relies on the relationship between measured peak positions and splittings to deduce secondary molecular structure or spin connectivity (*4, 5*). For tertiary structure, spatial relationships are obtained from homo- and heteronuclear dipolar couplings measured from contributions to spin relaxation rates by the nuclear Overhauser effect (nOe) (*5, 6*). Therefore, by judicious choice of one-, two-, and *n*-dimensional pulse sequences in conventionally available magnetic fields ($B_0 > 7$ T), a picture of molecular structure in the liquid state can be obtained (*7*).

As originally suggested by Sears and Hahn (*8*) and later successfully accomplished experimentally by Hilbers and MacLean (*9*), polar molecules in liquid samples can be aligned with an electric field E and examined by NMR. Our initial interest in this area was to judge whether or not electric field alignment could be used to improve the resolution of NMR through measurement of residual E field dependent dipolar and quadrupolar couplings in both organic and low ionic strength aqueous solutions of biological macromolecules. Toward this goal an NMR probe capable of launching up to 25 kV across a 3.6-mm electrode spacing was constructed. Perdeuterated nitrobenzene ($C_6D_5NO_2$) was chosen as an organic test sample because of its large dipole moment of 4.22 Debye, a high electrical breakdown threshold of >100 kV/cm, and the wide range of literature describing the behavior of nitrobenzene in electric fields (*10–13*). Simple one-dimensional (1D) deuterium ^{2}H NMR spectra for $C_6D_5NO_2$ as a function of voltage applied to the sample displayed splittings consistent with those previously observed (*9, 10, 14*), indicating molecular alignment and recovery of anisotropic spectral features as anticipated. Before extending to other samples, we realized that most interesting molecules will display extremely congested 1D NMR data and in the case of dipolar coupled $I = \frac{1}{2}$ nuclei, can become twice as complex in an aligned sample. In anticipation of this problem, one might be tempted to design a pulse sequence that separates this information into several spectral dimensions. In the course of applying the usual multiple rf pulse sequences capable of correlating anisotropic effects such as those induced with an E field with the usual liquids high-resolution spectrum, a serious problem became evident. It was noticed that the spin-echo generated by a $\pi/2 - \tau - \pi$ sequence was attenuated and, in most cases, eliminated with application of nonzero E fields. In fact, the echo reflecting $\tau =$ 30 ms could be attenuated by about an order of magnitude by applying a field of only 1 kV/cm to the sample. As a comparison direct spectral splittings in 1D spectra only begin to become resolved in 5 Hz wide ^{2}H lines when 15 kV/cm is applied to the sample. A clue to the source of the echo attenuation comes from two different measurements of the rate of recovery of the ^{2}H z magnetization to equilibrium as a function of the E field. The inversion recovery experiment yielded an E field independent relaxation rate, whereas the rate determined from a stimulated echo sequence decreased at higher E fields. This difference suggests that the echo attenuation must be due to electrically dependent molecular motion on the time scale of the NMR experiment, an observation corroborated by slight line narrowing observed in the ^{2}H NMR spectra of nitrobenzene at high E field (*10, 14*). Unfortunately, one could imagine

[1] To whom correspondence should be addressed.

1090-7807/00 $35.00

that if there is no signal following a spin echo sequence applied to a sample in a high *E* field due to this convective motion, then application of any common multidimensional NMR pulse sequence involving many rf pulses will simply not work. It is therefore necessary to design pulse sequences capable of compensating for the effect of the motion on the observed signal, a goal that requires better understanding of electrically induced convection in dielectric liquids.

It is well known that molecular motion may occur in insulating liquids under electrical stress. There are several potential sources of this electrohydrodynamic or electroconvective phenomenon such as thermal gradients due to Joule heating, dielectrophoresis of polar or polarizable particles due to strong *E* field gradients, and electrophoresis of charged species (*15*). In an effort to investigate the nature and source of motion in the case of polar organic solutions, magnetic resonance imaging (*16*) was used due to its unique ability to image the spatial distributions of molecules in time.

EXPERIMENTAL

Perdeuterated nitrobenzene ($C_6D_5NO_2$) 99.5% and perdeuterated benzene (C_6D_6) 99.5% were obtained from Aldrich and used without further purification. All ^{2}H NMR spectra were recorded at 45.37 MHz using a home-built NMR spectrometer controlled by a Tecmag Orion pulse programmer and constructed around an Oxford Instruments 89-mm diameter room temperature bore 6.95 T superconducting solenoid magnet. A sketch of the home-built probe head showing the relative positions of the sample cell, the rf coil consisting of two 20 mm long × 13 mm wide rectangular coils wrapped around a 17-mm diameter coil form, and the tuning and matching capacitors is presented in Fig. 1. The Maxwell pair along the *z* axis consisting of two 4-cm diameter 5 turn circular coils separated by 2 cm establishes a static linear field gradient parallel to the static magnetic field. Typically these coils are driven by 4 amps provided by a Sorensen 12 V/30 A power supply, thereby establishing a 1.0 G/cm magnetic field gradient across a 3.6-mm sample. Both gradient and rf coil forms as well as the electric field cell were machined from polyphenylene sulfide (PPS), a material with outstanding resistance to chemical reaction and with nearly the same magnetic susceptibility as both nitrobenzene and water. Although not important for this study, the choice of PPS as support material is critical to the minimization of sample end effects and the consequential minimization of spectral linewidths. The electric field cell used in this study is completely removable from the probe head as illustrated by its position in Fig. 1, and the 12 mm diameter × 0.5 mm long cylindrical electrodes were made of polished copper. In all cases the cell is filled with liquid outside of the probe, sleeved vertically from the probe base through a series of 1-inch holes, and finally suspended by connecting the cathode to the ground plane at the top of the probe. In this way, the 3.6 mm long × 11 mm diameter cylindrical sample volume

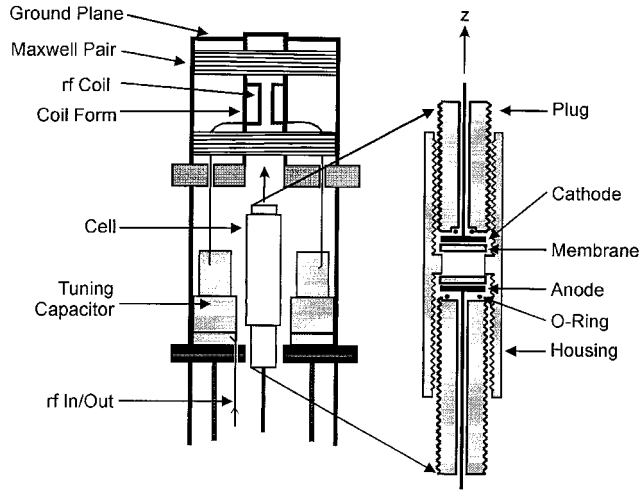

FIG. 1. NMR probe and electric field cell (not drawn to scale) used in this study. The tank circuit in the probe head on the left is tuned to the Larmor frequency for ^{2}H, and the Maxwell pair along the *z* axis establishes a linear magnetic field gradient for imaging. The electric field cell is inserted into the probe head from bottom to top and suspended within the rf coil form. The exploded view on the right shows the PPS electric field cell with the copper electrodes shown in black. As mentioned in the text, the components critical to successful operation of the cell are the ion purification membranes and the o-ring gasketted plugs.

is centered within the rf coil. The relative position of the sample volume to the electrodes and other critical cell components can be seen in the exploded view of the cell on the right-hand side of Fig. 1. Here the anode is connected through the bottom of the probe to a Bertan Model 210–50R power supply by high voltage cable. Electrical breakdown from the anode to the surrounding rf coil and ground planes was eliminated by shielding the high-voltage cable with an automobile spark plug insulator and by removing any sample filling holes from the cell. The absence of filling ports required the use of 18 mm long × 12.5 mm diameter cylindrical o-ring equipped plugs that could be threaded into the main sample housing. Upon making contact with the ledge machined in the main housing, an o-ring seal could be made between the back face of the electrode and the plug, preventing any sample leakage. The cell design in Fig. 1 incorporates two features necessary to ensure successful alignment of molecules by *E* fields that are not immediately obvious. The gasketted/threaded plugs allow bubble-free filling of the cell. Since the dielectric constant for air is much less than that of a liquid sample, electrical breakdown in the cell is much easier when bubbles are present resulting in unreasonably low upper limits to the *E* field established across a sample. Also, bubbles have the unpleasant effect of broadening NMR lines. The second feature is the presence of ionic membranes separating the electrodes from the sample solution. The polypropylene cationic (CR67LMP-447) and anionic (AR103-QDP) membranes were obtained from Ionics, Incorporated. Their purpose as first recognized by Brière *et al.* (*11–13*) is to remove ionic impurities from the

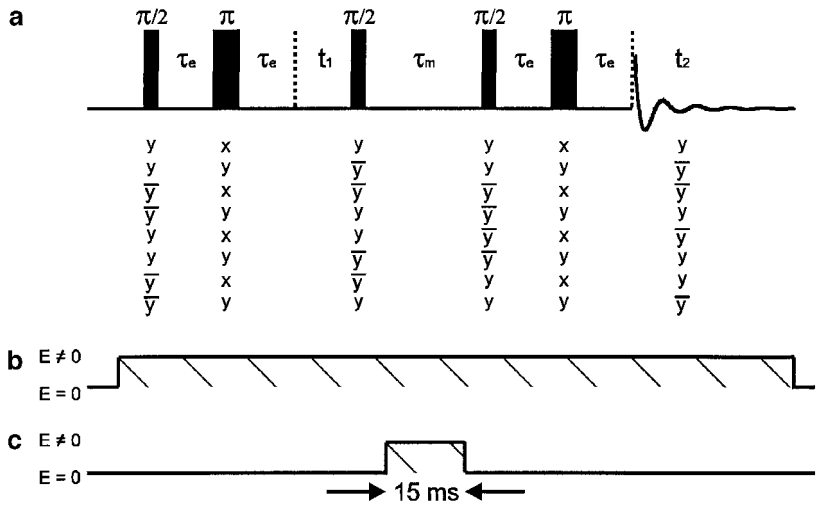

FIG. 2. Magnetic resonance imaging pulse sequence used in this study. The rf pulse timing diagram in (a) typically employs $\tau_e = 500$ μs and a variable mixing time τ_m in the case of a continuous electric field in (b) and $\tau_m = 100$ ms for a pulsed electric field in (c). In all experiments, the magnetic field gradient $G_z = 1.0$ G/cm remains on for the entire duration of the measurement. As noted in (c) the electric field pulse lasts only 15 ms and is centered on the $\tau_m = 100$ ms mixing time shown in (a). The eight-step phase cycle in (a) is designed to select only the image correlation signal.

solution. In the case of nitrobenzene, it is known that a small percentage of water can form nitrophenol that readily ionizes (*13*) resulting in an unreasonably high sample conductivity $\sigma \approx 10^{-7}$ $(\Omega\ \text{cm})^{-1}$. Unfortunately, electropurification of nitrobenzene is not instantaneous. It was found that gradually increasing the field to operating values of 30–40 kV/cm over the course of several hours gave the purest solutions having $\sigma \approx 5 \times 10^{-11}$ $(\Omega\ \text{cm})^{-1}$ as suggested from the cell geometry and by the decrease in current flow in the cell from more than 1 mA to less than 1 μA for a constant 2.5 kV potential. Without these membranes, fluctuations due to ion currents within the sample minimize the effect of the *E* field, and NMR spectral effects are washed out. Experiments requiring gated *E* fields were accomplished by placing a TTL controlled Kilovac K62C-841 25 kV relay between the cell and power supply. Here, the sample was purified over the course of several hours and the field was briefly gated when required as dictated by the appropriate imaging pulse sequence. In order to remain consistent with earlier experiments on $C_6D_5NO_2$ (*9–14*), all reported *E* field values were determined by dividing the voltage applied to the electrodes by their separation of 3.6 mm.

RESULTS

The cylindrical symmetry of the cell shown in the exploded view in Fig. 1 greatly simplifies the pulse sequence needed to explore electrically induced convection in $C_6D_5NO_2$. The pulse sequence in Fig. 2 was used to monitor the effect of both continuous and pulsed *E* fields on $C_6D_5NO_2$ by correlating the ^{2}H 1D image of the cell with itself at two times separated by the mixing time τ_m. The π pulses refocus the signal to minimize phasing artifacts in the resulting two-dimensional (2D) spectrum. Typically $\tau_e = 500$ μs because as we shall see most motional effects occur on a time scale greater than 5 ms. The third rf pulse of tipping angle $\pi/2$ rotates a component of the transverse magnetization to the *z* direction at a time t_1 after formation of the first spin-echo at $2\tau_e$ following the initial $\pi/2$ pulse. Next, the *z* magnetization corresponding to a set of spins for one molecule is transported by either a continuous *E* field shown in Fig. 2b or a pulsed *E* field in Fig. 2c to a different region of the cell prior to the detection echo sequence at a time τ_m later. The phase cycle in Fig. 2a cancels any unwanted free induction and echo signals due to rf inhomogeneity and imperfect tipping angle rf pulses. When combined with time proportional phase incrementation (*17*) on the first pulse and following Fourier transformation with respect to both t_1 and t_2, a correlation between images is obtained. Figure 3a shows this image correlation in $C_6D_5NO_2$ for $\tau_m = 20$ ms and $E = 0$ kV/cm. Projection along either the directly detected $z(\tau_m)$ or indirectly detected $z(0)$ axis recovers the anticipated ^{2}H 1D image of liquid $C_6D_5NO_2$. Here, and in all images obtained in this study, $G_z = 1.0$ G/cm as can be seen from the axis labels in Fig. 3a where the frequency to distance scaling factor is 2.4 mm/kHz. This diagonal correlation spectrum obtained with a zero *E* field indicates that there is minimal motion on the time scale of $\tau_m = 20$ ms. At a shorter mixing time $\tau_m = 1$ ms and at an *E* field of 9.6 kV/cm, the correlation spectrum begins to broaden as shown in Fig. 3b. Leaving the field fixed at this value and increasing τ_m to 3, 5, 10, and 20 ms yields the image correlation spectra shown in Figs. 3c, 3d, 3e, and 3f, respectively. Similar image correlation spectra were obtained with a gated variable-amplitude *E* field placed in the middle of a fixed $\tau_m = 100$ ms delay as shown schematically in the timing

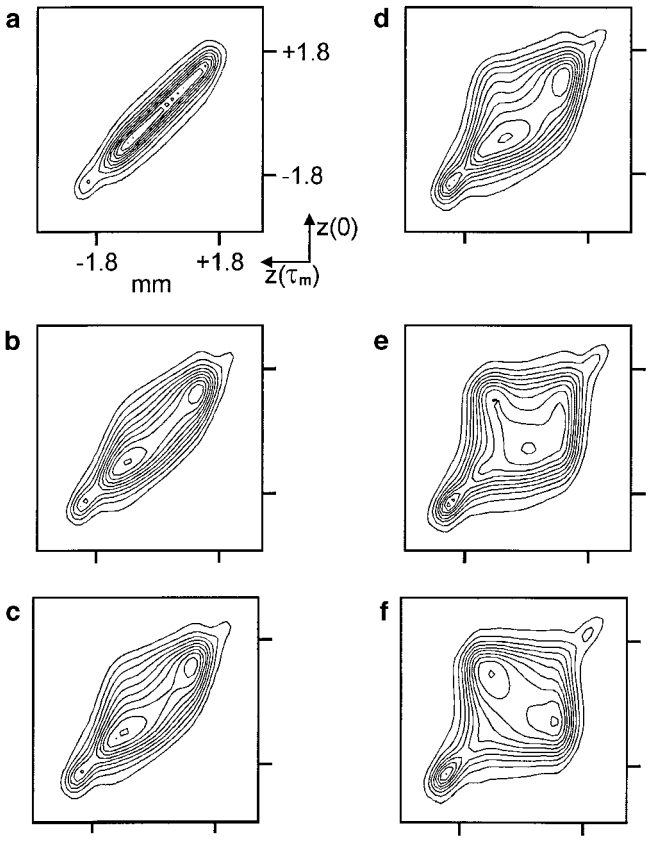

FIG. 3. Image correlation spectra obtained under conditions of continuous E field and for different mixing times τ_m. In (a) $E = 0$ while in (b)–(f) $E = 9.6$ kV/cm. In (a) $\tau_m = 20$ ms while τ_m was 1 ms in (b), 3 ms in (c), 5 ms in (d), 10 ms in (e), and 20 ms in (f). Identical spectral regions are shown in each plot; therefore, the axis labels shown in (a) apply to all image correlation spectra shown in the figure. The inset axes shown in the lower right of (a) apply to all image correlation spectra and reflect the directly detected $z(\tau_m)$ and the indirectly detected $z(0)$ dimensions.

diagram in Fig. 2c. The results of this pulse sequence as a function of E field amplitude for a constant 15-ms pulse are shown in Fig. 4. As in Fig. 3a the $E = 0$ kV/cm correlation spectrum in Fig. 4a reflects only Brownian motion during the course of the experiment. It is important to note that comparison between the width of the contours along the line with a slope of -1 in Figs. 3a and 4a is meaningless as different contours are shown for display purposes. Increasing the E field while keeping the pulse duration fixed at 15 ms yields image correlation spectra like those shown in shown in Figs. 4b, 4c, 4d, 4e, and 4f for 2.7, 5.5, 8.3, 11.0, and 13.8 kV/cm, respectively. The results of applying the same gated E field image correlation sequence to C_6D_6 and mixtures of $C_6H_5NO_2$ and C_6D_6 are shown in Fig. 5. In Fig. 5a the image correlation spectrum of C_6D_6 for $E = 13.8$ kV/cm is presented. Keeping the gated E field fixed while increasing the volume ratio of $C_6H_5NO_2/C_6D_6$ to 9% and 27% produce the spectra shown in Figs. 5b and 5c, respectively.

DISCUSSION

Nitrobenzene Correlation Spectra

Three features in the spectra shown in Fig. 3 immediately become evident. The evolution from primarily a diagonal to square spectrum suggests that by $\tau_m = 10$ ms a given molecule has sampled virtually every magnetic environment within the electric field cell in a random fashion and that the motion is on the tens of milliseconds time scale. Since the magnetic field gradient is linear, this observation indicates that each molecule has traversed the entire cell in at most 20 ms as shown in Fig. 3f. Another interesting characteristic of these spectra is the peculiar lack of motion at the ends of the sample illustrated most clearly in Fig. 3f by the absence of any cross peaks between molecules above +1.8 mm and those below −1.8 mm. This feature reflects the restricted motion of $C_6D_5NO_2$ molecules both imbedded within the membranes and trapped between the membranes and electrodes. The remainder of the

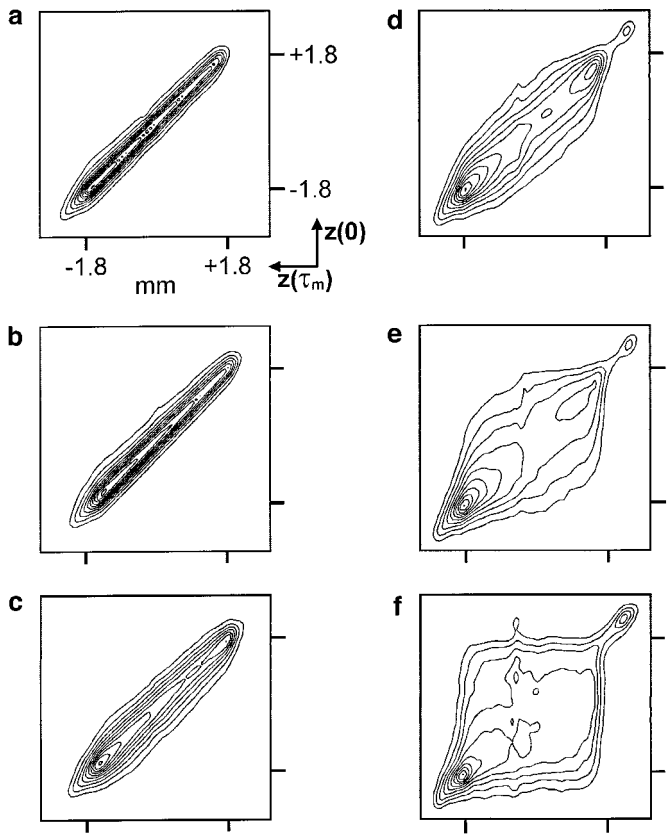

FIG. 4. Image correlation spectra obtained using a pulsed E field for $\tau_m = 100$ ms and pulse length of 15 ms. The intensity of the electric field was increased from $E = 0$ kV/cm in (a) to 2.8 kV/cm in (b), 5.5 kV/cm in (c), 8.3 kV/cm in (d), 11.0 kV/cm in (e), and 13.8 kV/cm in (f). Again, identical spectral regions are shown in each plot; therefore, the axis labels shown in (a) are appropriate for all image correlation spectra shown in the figure. Also, the inset axes shown in the lower right of (a) apply to all image correlation spectra and reflect the directly detected $z(\tau_m)$ and the indirectly detected $z(0)$ dimensions.

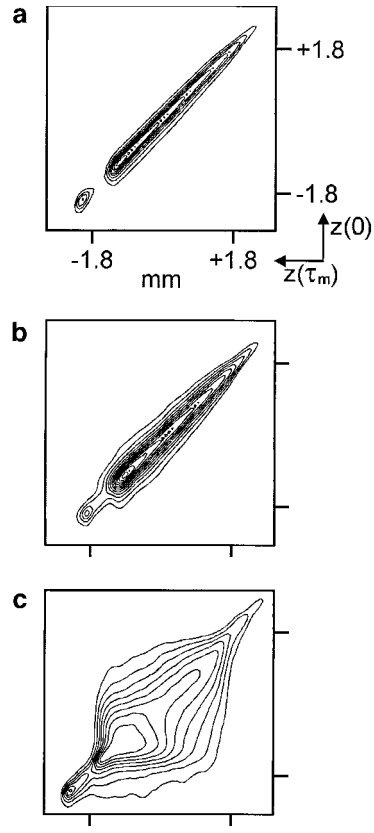

FIG. 5. Image correlation spectra obtained using the same conditions as in Fig. 4 and $E = 13.8$ kV/cm. The diagonal spectrum in (a) corresponds to pure C_6D_6 while (b) and (c) reflect motion initiated by adding 9 and 27% volume ratios of $C_6H_5NO_2/C_6D_6$, respectively. Regardless of $C_6H_5NO_2$ concentration, a 0.3 μA current was observed.

liquid $C_6D_5NO_2$ moves freely and yields the square correlation spectrum in Fig. 3f. The final feature to note is the increased cross peak intensity between ± 1.8 and ∓ 1.8 mm in the correlation spectra, most noticeable in Fig. 3f. Since all of the spectra in Fig. 3 were obtained under conditions of a continuous E field of 9.6 kV/cm and because the 1D magnetic resonance image acquired following one rf pulse does not display this property, the increased intensity can be attributed to edge enhancement of the image (*18*). This enhancement increases with molecular motion and is amplified by the spin-echo encoding and detection events in the pulse sequence shown in Fig. 2a.

In order to investigate molecular motion imposed by an E field while preventing motional edge enhancement, the continuous field in Fig. 2b was replaced by a gated E field. In this experiment, the E field pulse initiates a positional exchange and the spin-echo encoding and detection events occur under conditions of minimal molecular motion while the field is gated off. Again, the evolution from primarily a diagonal to square correlation spectrum suggests that for the higher applied fields, a given molecule has sampled all magnetic environments in the cell during exposure to the E field for just 15 ms. These results are consistent with the time scale of motion anticipated from Fig. 3. The results of some representative applied fields in Fig. 4 again show evidence of liquid trapped in the membranes and between the membranes and electrodes, but perhaps more importantly these spectra do not display characteristics indicative of the image edge enhancement seen in Fig. 3.

Source of the Motion

It is common for conducting liquids to experience Joule heating upon application of electric current. Because such heating may establish thermal gradients within the liquid which may in turn cause fluid flow, it is important to consider it as a possible source of motion. The rate of temperature change for a liquid as a function of temperature T, conductivity σ, density ρ, specific heat at constant pressure C_p, and applied electric field is (*19*)

$$\frac{dT}{dt} = \frac{\sigma E^2}{\rho C_p}. \qquad [1]$$

Substitution of the appropriate values for $C_6D_5NO_2$ ($C_p = 178$ J/mol K, $\sigma = 5 \times 10^{-11}$ $(\Omega\ \text{cm})^{-1}$, $\rho = 1.2037$ g/cm^3) at room temperature and $E = 13.8$ kV/cm into Eq. [1] gives $dT/dt = 2 \times 10^{-3}$ K/s. This rate translates into an increase in temperature of 3×10^{-5} K during the 15 ms electric field pulse used in Fig. 4. To experimentally verify that the Joule heating corresponding to this temperature jump insignificantly contributes to molecular motion, image correlation spectra for C_6D_6 and mixed solutions of C_6D_6 and $C_6H_5NO_2$ were obtained. For pure C_6D_6 one expects the temperature change for the same 15 ms pulse to be only a factor of two less than that for pure $C_6D_5NO_2$ on the basis of the current flow in the cell being 0.3 μA at $E = 13.8$ kV/cm or $\sigma \approx 2 \times 10^{-11}$ $(\Omega\ \text{cm})^{-1}$. In fact, on the basis of a Joule heating mechanism for molecular motion and experimental observation of constant cell current and thus fixed conductivity for low concentrations of $C_6H_5NO_2$ in C_6D_6, one would expect the image correlation spectra in Fig. 5 to be identical. Clearly application of an E field to just C_6D_6 causes minimal positional exchange as seen in Fig. 5a, whereas incorporation of $C_6H_5NO_2$ introduces molecular motion in Figs. 5b and 5c, which is in disagreement with a Joule heating model for this electrohydrodynamic motion.

Electroconvection in a dielectric liquid may also be observed when dipolar or polarizable molecules are subjected to strong static electric field gradients ∇E. Here, molecules of dipole moment p or polarizability α such that $p = \alpha E$ interact with the E field. The potential energy of this interaction $U = -\mathbf{p} \cdot \mathbf{E}$ can be used to determine a driving force for molecular motion $F = -\nabla U = p\nabla E$. This dielectrophoresis as pointed out by Pohl (*20*) is typically seen in bulk liquid samples only under special conditions of strongly divergent E fields, e.g., the tip of a high voltage wire held close to the surface of a liquid. Kerr effect studies of nitrobenzene under experimental condi-

tions similar to ours (i.e., electrode geometry and spacing and field strength) indicate that gradients $1 < \nabla E < 10$ kV/cm^2 do indeed exist (*21, 22*), but as mentioned by Pohl, are not of sufficient magnitude for dielectrophoresis in bulk liquids to be appreciable. This contention was confirmed experimentally by the application of AC potentials. Since dielectrophoresis depends on E^2, application of an AC field having a mean square value similar to the DC field here can be used to probe this motion. One must be clear that electrophoretic motion of charged particles proceeds by a different mechanism that is proportional to E and ceases at sufficiently high AC field frequency (*15*). The absence of the effects of electroconvection on the NMR spectra of $C_6D_5NO_2$ upon application of an AC field strongly suggests that dielectrophoresis is not the source of 10 ms time scale motion in $C_6D_5NO_2$ (*23*).

The most likely cause of molecular motion in polar organic solutions as discussed in detail by Croitoru is the formation of "space charges" (*24*). In dielectric liquids, space charges exist as ionic impurities formed by electrolysis or by direct electrode or membrane injection. The electrophoretic forces on these space charges proportional to E as mentioned above leads to molecular motion. Basically, molecules with dipole moments aggregate around the injected charge to maintain neutrality. Equivalently one can imagine that the intense short-range electric field generated by the point charge polarizes the surrounding dipole moments. While formation of space charges due to electrolysis and decomposition can be understood using principles of electrochemistry and organic chemistry, mechanisms of millisecond time scale space charge creation and annihilation by charge injection are not well understood. It is thought to be the result of electron exchange occurring at the interface of a dielectric and the surface of metallic electrodes or charged membranes. Embodied in this model is space charge creation at the cathode and annihilation at the anode. The existence of space charges are frequently used to explain the presence of nonuniform E fields as measured by the Kerr effect in dielectric liquids (*24*) including nitrobenzene under experimental conditions similar to those used here (*21, 22*). The absence of convective effects in nitrobenzene upon application of AC fields mentioned above is consistent with space charge formation. On one hand, the periodic reversal of E field forces the charge to oscillate about its initial position, while on the other hand, the oscillation frequency is too high to establish uniform injection of charge. In addition, the results in Fig. 5 can be easily explained within the framework of space charge formation. As pointed out by Croitoru, charge injection of electrodes is higher in liquids of higher permittivity ϵ. Since ϵ in $C_6H_5NO_2$ is nearly 15 times that for C_6D_6, space charges more readily form in $C_6H_5NO_2$. As the fraction of $C_6H_5NO_2$ increases in $C_6H_5NO_2/C_6D_6$ binary mixtures, one would expect the formation of more space charges and the presence of more molecular motion as seen in Fig. 5.

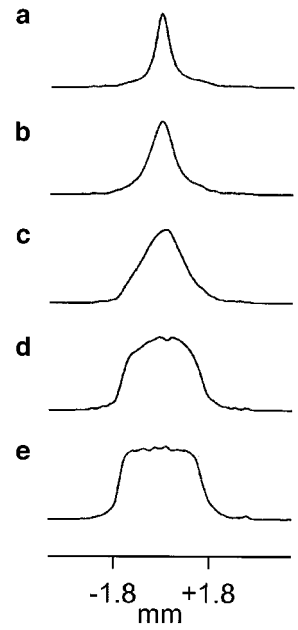

FIG. 6. Molecular position distributions extracted from the pulsed electric field image correlation spectra in Fig. 4. The data in (a), (b), (c), (d), and (e) directly correspond to the horizontal $z(0) = 0$ mm slices extracted from the spectra in Fig. 4b, 4c, 4d, 4e, and 4f, respectively.

Characterizing the Motion

The nature of this electrophoretic space charge motion can be further probed by taking advantage of the ability of magnetic resonance imaging to examine spin concentration profiles. First, a few qualitative conclusions may be drawn by looking at Figs. 3 and 4. In similar 2D NMR experiments like spin-diffusion measurements in solid samples (*25*) or experiments involving chemically exchanging systems (*26*), there is no requirement for cross-peaks symmetrically disposed about the diagonal of the spectrum to have equal intensity (*4*). In Figs. 3f and 4f, however, image correlations are observed with equal cross-peak intensity suggesting that molecules are traveling from one side of the cell to the other. Furthermore, the box-like feature of the images shows that molecules have been evenly distributed throughout the cell due to the E field. This observation is consistent with the dispersive nature of turbulent flow expected for the continually developing concentration of space charges within the sample.

A more descriptive analysis may be achieved by extracting a 1D slice of the 2D data corresponding to molecules in the sample having an initially identical magnetic field. Physically, this slice corresponds to all molecules within a disk-like area at a given position z in the cell shown in Fig. 1. The slices shown in Figs. 6a–6e were obtained by extracting the $z(0) = 0$ slices from Figs. 4b–4f, respectively. These slices correspond directly to molecules initially located at the center of the sample. Figure 6a corresponds to a distribution function of the positions of molecules following application of a 15 ms $E = 2.8$ kV/cm

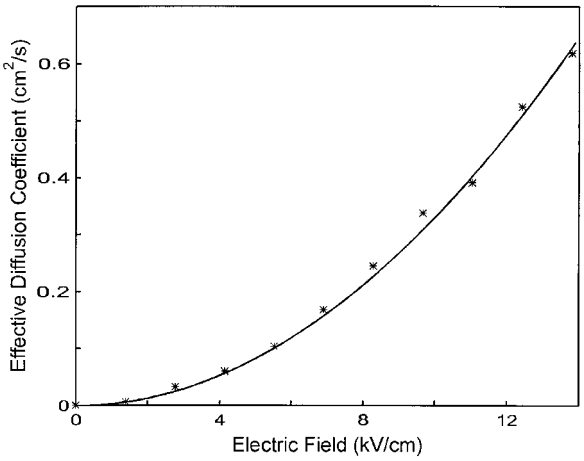

FIG. 7. Dependence of the effective diffusion coefficient D (*) on the applied E field as determined by comparing slices like those in Fig. 6 to Eq. [2]. The solid line represents a best fit solution to Eq. [3] while holding $D^{(0)}$ to the self diffusion value of 1.08×10^{-5} cm^2/s, $D^{(1)} = 0$ cm^3/kVs, and varying $D^{(2)}$ to the minimum value of 6.66×10^{-3} cm^4/kV^{2}s.

pulse and reveals a Gaussian position distribution. As the E field is increased, the width of this distribution increases as expected as the molecules move further in 15 ms under an increased E due to the increased electrophoretic force on the space charges. The slices in Figs. 6d and 6e reveal sample cell boundary effects as molecules under a larger E field begin to encounter the boundaries of the cell established by the membrane covered electrodes. It is not surprising that the slices in Fig. 6 resemble solutions of the diffusion equation with parallel plane boundary conditions since the random dispersion of particles in turbulent flow is very similar to molecular diffusion. The solution for the Fokker–Planck probability for 1D diffusion bounded at $\pm l/2$ given a delta function initial probability distribution centered at $z(0)$ is (*27*)

$$P[z(\tau_m), z(0); \tau_m] = (1/l) + \sum_{n>0} (2/l)\cos[n\pi z(\tau_m)/l] \times \cos[n\pi z(0)/l]\exp[-(Dn^2\pi^2/l^2)\tau_m]. \quad [2]$$

Here D is the diffusion coefficient we wish to determine and $P[z(\tau_m), z(0); \tau_m]$ is the probability that a particle at position $z(0)$ at time $t = 0$ diffuses to position $z(\tau_m)$ at time $t = \tau_m$. By setting $z(0) = 0$ mm and $t = \tau_m = 15$ ms in Eq. [2], D can be determined for each E field choice in Fig. 6 by calculating a best-fit position distribution of particles initially located at $z(0) = 0$ mm, the center of the E field cell. It should be clear that the diffusion coefficient used here is just an effective parameter used to characterize the turbulent flow generated by electrophoresis of space charges. The precise dependence of D on E extracted from this model and shown in Fig. 7 can be obtained from the Taylor expansion

$$D = D|_{E=0} + \left.\frac{dD}{dE}\right|_{E=0} E + \frac{1}{2}\left.\frac{d^2D}{dE^2}\right|_{E=0} E^2 \ldots$$

$$D = D^{(0)} + D^{(1)}E + \frac{D^{(2)}}{2}E^2 \quad [3]$$

and regression to the data in Fig. 7. By allowing full parameter variation, a generic second-order polynomial fit yields $D^{(0)} = -3.93 \times 10^{-3}$ cm^2/s, $D^{(1)} = 4.80 \times 10^{-3}$ cm^3/kVs, and $D^{(2)} = 5.91 \times 10^{-3}$ cm^4/kV^{2}s with an R^2 value of 0.998. This unphysical negative value of $D^{(0)}$ combined with the minimal contribution of the gradient term $D^{(1)}$ to the overall effective diffusion coefficient at the high fields used here, on the order of $D^{(1)}E/D \approx 0.1$ at $E = 10$ kV/cm, prompts refitting of the data while constraining $D^{(1)}$ to zero. This approximation yields a similar R^2 value of 0.997 while giving $D^{(0)} = 7.68 \times 10^{-3}$ cm^2/s and $D^{(2)} = 6.55 \times 10^{-3}$ cm^4/kV^{2}s. Further refinement in our interpretation of this data can be realized by using the $E = 0$ kV/cm data slice from Fig. 4a to fix $D^{(0)}$ at 6.88×10^{-4} cm^2/s. Redetermination of $D^{(2)}$ as 6.69×10^{-3} cm^4/kV^{2}s while holding $D^{(1)} = 0$ cm^3/kVs gives $R^2 = 0.996$. Regardless of the regression procedure and level of approximation, all values for $D^{(0)}$ significantly differ from the actual coefficient for nitrobenzene self diffusion of $D^{(0)} = 1.08 \times 10^{-5}$ cm^2/s (*28*). Fortunately, this discrepancy only reflects the resolution limit of the experimental measurement and approximations used to interpret the data in Fig. 6. For Brownian motion in $C_6D_5NO_2$, the rms displacement in the $\tau_m = 100$ ms period corresponds to a distance of $(Dt)^{1/2} \approx 10$ μm, a linewidth below the 90 μm/pt resolution of the experiment. The linewidth present in the $E = 0$ kV/cm data slice and discrepancy between $D^{(0)}$ values mentioned above are simply a reflection of the combined interplay of relaxation times, data apodization, and inadequate spectral resolution. It is for these reasons that this type of data does not provide an accurate measurement of $D^{(0)}$ at low E field. At higher E fields, the effect of motion dominates these limits set by inherent and imposed linewidth and spectral resolution. In order to recover a physical $E = 0$ kV/cm value for D, the data shown in Fig. 7 was refit using the actual self diffusion value for nitrobenzene of $D^{(0)} = 1.08 \times 10^{-5}$ cm^2/s and the approximation that $D^{(1)} = 0$ cm^3/kVs. This regression gave $D^{(2)} = 6.66 \times 10^{-3}$ cm^4/kV^{2}s with an R^2 value of 0.996, values represented by the solid line in Fig. 7. Since it is in this regime where NMR measurements of aligned molecules are performed and the R^2 value is high using the proper $E = 0$ kV/cm coefficient for self diffusion, assignment of $D^{(2)}$ as 6.66×10^{-3} cm^4/kV^{2}s can be considered a reasonable estimate.

Finally, the E^2 dependence of D measured here is an important result. The charge velocity in turbulent flow generated by space charge electrophoresis depends linearly on E (*29, 30*) dictating that the mean square charge velocity is proportional to E^2. This dependence is borne out in the measurement of D here since, from diffusion theory, the mean square velocity is proportional to D/t and hence E^2.

CONCLUSIONS

The purpose of this study was to identify the source of and characterize electroconvection in a polar nonaqueous solvent in order to develop NMR pulse sequences that compensate for the effect. To address this problem, magnetic resonance imaging pulse sequences capable of correlating 1D images recorded at two different times were designed and applied to $C_6D_5NO_2$ in both continuous and pulsed electric fields. The results indicate that the motion observed in the image correlation spectra is caused by electrophoretic forces acting on ionic electrolysis products and injected charges in the liquid, not from thermal gradients due to Joule heating or from dielectrophoretic movement of dipolar molecules in E field gradients. This motional process is observed to be consistent with turbulent flow and is similar to an amplified bounded diffusion process whose electric field dependent effective diffusion coefficient is given by $D = 1.08 \times 10^{-5}$ cm^2/s + $\frac{1}{2}$ (6.66×10^{-3} cm^4/kV^{2}s) E^2. The E^2 dependence of mean square velocity inferred from the same dependence of D agrees with the literature for turbulent electroconvection. The primary limitation of this imaging approach to characterizing turbulent flow in organic solution is the background Brownian motion of the molecules themselves. Incorporation of pulsed magnetic field gradients (*31*) coupled with electric field pulses would remove this limitation; however, this was not done in the current study because of the long ring-down time of the home-built Maxwell coil. Clearly, pulsed field gradients would permit a more accurate measure of the correlation time and/or length for local motion.

The diffusive, random, and stochastic nature of the motion combined with its observed tens of millisecond time scale suggest one way of compensating for these effects in pulsed NMR experiments performed in an electric field. Since this process appears similar to diffusion which imparts a τ^3 dependence on the amplitude of the $\pi/2 - \tau - \pi$ spin echo (*32*), one can apply the method of Carr and Purcell (*33*) to attenuate its effect. Here, one basically applies a train of π pulses separated by a time less than the time scale of the molecular motion. For the experiments discussed above in 1–15 kV/cm electric fields, one must simply space the π pulses by less than 5 ms in order to significantly attenuate and even eliminate motional effects on the multiple rf pulse observable magnetization. By using an approach like this to minimize artificial signal loss due to electroconvection, one may be able to record n-dimensional NMR spectra under conditions of both continuous and pulsed electric fields to extract useful molecular structure parameters. The success of such experiments will ultimately lead to more refined liquid state molecular structure as determined by NMR.

Previous investigations of electroconvection have used both direct (light scattering off dust particles, photography of polyethylene particles, use of colored dyes or air bubbles) and indirect (schlieren photographs or laser doppler velocimetry of light scattering particles) methods of liquid flow visualization. Unfortunately, all of these methods with the exception of the schlieren technique require an additive to the liquid under investigation that may alter the electrolytic properties of the liquid. While schlieren photographs are sensitive to small variations in the refractive index of the liquid and allow macroscopic observations of electroconvective motion as was beautifully demonstrated by Hopfinger and Gosse (*34*), they do not allow a microscopic measurement of particles undergoing steady state turbulent flow. This study has demonstrated the usefulness of magnetic resonance imaging in making microscopic observations of electroconvection. It is interesting to consider extending the dimensionality of the imaging from one dimension to three in order to investigate the three-dimensional flow of particles in an electric field. Furthermore, the method used here may be modified to utilize modern techniques of flow imaging using pulsed gradients to obtain velocity and diffusion maps of electroconvection (*31*).

Having fulfilled the primary goal of this work, it is also interesting to speculate toward other useful experiments at the interface of magnetic resonance imaging and electric field oriented molecules. NMR measurements made elsewhere (*35*) suggest that certain ferroelectric liquid crystal side chains undergo interesting motion in the presence of an electric field. One could imagine a direct measure of this motion by replacing the simple Maxwell pair in Fig. 1 with a gradient set capable of launching massive 600 T/m field gradients across the sample such as those used by Zhang and Cory (*36*). By increasing the resolution of this imaging experiment from 2 μm/Hz to 40 pm/Hz an accurate real-time and real-length scale picture of ferroelectric polymer dynamics in an electric field could be obtained.

ACKNOWLEDGMENTS

The authors are indebted to both Erwin Hahn and Jeff Reimer for stimulating conversation and continued encouragement throughout the course of this work. This work was supported by the National Science Foundation under Grant CHE-9504655, the Packard Foundation, and U.C. Davis.

REFERENCES

1. C. R. Cantor and P. R. Schimmel, "Biophysical Chemistry. Part II: Techniques for the Study of Biological Structure and Function," Freeman, New York (1980).
2. R. M. Silverstein, G. C. Bassler, and T. C. Morrill, "Spectrometric Identification of Organic Compounds," Wiley, New York (1981).
3. R. K. Harris, "Nuclear Magnetic Resonance Spectroscopy: A Physiochemical View," Wiley, New York (1987).
4. R. R. Ernst, G. Bodenhausen, and A. Wokaun, "Principles of Nuclear Magnetic Resonance in One and Two Dimensions," Oxford University Press, New York (1997).
5. A. W. Overhauser, Polarization of nuclei in metals, *Phys. Rev.* **92,** 411 (1953).
6. K. Wuthrich, "NMR of Proteins and Nucleic Acids," Wiley, New York (1986).
7. C. P. Slichter, "Principles of Magnetic Resonance," Springer-Verlag, New York (1990).

8. R. E. J. Sears and E. L. Hahn, Upper limits to electric-field-induced magnetic dipole–dipole couplings in polar liquids, *J. Chem. Phys.* **45,** 2753 (1966).
9. C. W. Hilbers and C. MacLean, Electric field effects in NMR, *Chem. Phys. Lett.* **2,** 445 (1968).
10. C. W. Hilbers and C. MacLean, Electric field effects in nuclear magnetic resonance, *Mol. Phys.* **16,** 275 (1969).
11. G. Brière and B. Rose, Electrodialysis of polar solvents. VI. Ionic purification of aprotic liquids, *J. Chim. Phys.* **64,** 1720 (1967).
12. G. Brière and J. P. Gosse, Electrodialysis of polar solvents. VII. Ionic purification of nitrobenzene controlled by the simultaneous observation of electric field distribution and conduction current as a function of time, *J. Chim. Phys.* **65,** 1341 (1968).
13. G. Brière, G. Cauquis, B. Rose, and D. Serve, Relation between the electrical conductivity of pure polar liquids and their electrochemical properties for the case of nitrobenzene, *J. Chim. Phys.* **66,** 44 (1969).
14. P. C. M. van Zijl, B. H. Ruessink, J. Bulthuis, and C. MacLean, NMR of partially aligned liquids: Magnetic susceptibility anisotropies and dielectric properties, *Acc. Chem. Res.* **17,** 172 (1984).
15. W. F. Pickard, Electrical force effects in dielectric liquids, *in* "Progress in Dielectrics" (J. B. Birks and J. Hart, Eds.), Vol. 6, pp. 1–39, Academic Press, New York (1965).
16. P. T. Callaghan, "Principles of Nuclear Magnetic Resonance Microscopy," Oxford University Press, New York (1997).
17. G. Drobny, A. Pines, S. Sinton, D. Weitekamp, and D. Wemmer, Fourier transform multiple quantum nuclear magnetic resonance, *Faraday Div. Chem. Soc. Symp.* **13,** 49 (1979).
18. T. M. DeSwiet, Diffusive edge enhancement in imaging, *J. Magn. Reson. Ser. B* **109,** 12 (1995).
19. J. M. H. Peters, J. L. Sproston, and G. Walker, Preliminary observations on bulk electroconvection in electrically stressed liquid insulants Part I: Experimental Investigation, *J. Electrost.* **8,** 139 (1980).
20. H. A. Pohl, "Dielectrophoresis," Cambridge University Press, Cambridge (1978).
21. E. C. Cassidy and H. N. Cones, A Kerr electro-optical technique for observation and analysis of high-intensity electric fields, *J. Res. Natl. Bur. Stand., Sect. C* **73,** 5 (1969).
22. E. C. Cassidy, R. E. Hebner, Jr., M. Zahn, and R. J. Sojka, Kerr-effect studies of an insulating liquid under varied high-voltage conditions, *IEEE Trans. Electr. Insul.* **9,** 43 (1974).
23. A. Peshkovsky and A. E. McDermott, NMR spectroscopy in the presence of strong AC electric fields: Degree of alignment of polar molecules, *J. Phys. Chem. A* **103,** 8604 (1999).
24. Z. Croitoru, Space charges in dielectrics, *in* "Progress in Dielectrics" (J. B. Birks and J. Hart, Eds.), Vol. 6, pp. 103–146, Academic Press, New York (1965).
25. K. Schmidt-Rohr and H. Speiss, Chain diffusion between crystalline and amorphous regions in polyethylene detected by 2D exchange ^{13}C NMR, *Macromolecules* **24,** 5288 (1991).
26. J. I. Kaplan and G. Fraenkel, "NMR of Chemically Exchanging Systems," Academic Press, New York (1980).
27. C. H. Neumann, Spin echo of spins diffusing in a bounded medium, *J. Chem. Phys.* **60,** 4508 (1974).
28. E. Hawlicka and W. Reimschüssel, Self-diffusion of components in aniline-benzene solution, *Ber. Bunsenges. Phys. Chem.* **84,** 1119 (1980).
29. G. A. Ostroumov, Hydrodynamics of electrical discharges, *J. Tech. Phys. (U.S.S.R)* **24,** 1915 (1954).
30. N. Felici and J. C. Lacroix, Electroconvection in insulating liquids with special reference to uni- and bipolar injection, *J. Electrost.* **5,** 135 (1978).
31. P. T. Callaghan, "Principles of Nuclear Magnetic Resonance Microscopy," Clarendon Press, Oxford (1991).
32. E. L. Hahn, Spin echoes, *Phys. Rev.* **80,** 580 (1950).
33. H. Y. Carr and E. M. Purcell, Effects of diffusion on free precession in nuclear magnetic resonance experiments, *Phys. Rev.* **94,** 630 (1954).
34. E. J. Hopfinger and J. P. Gosse, Charge transport by self-generated turbulence in insulating liquids submitted to unipolar injection, *Phys. Fluids* **14,** 1671 (1971).
35. P. Holstein, A. C. D. Lopes, J. Rauchfuss, and D. Geschke, ^{1}H multiple-pulse solid-state NMR investigations of electrically oriented liquid crystals, *Magn. Reson. Chem.* **35,** 420 (1997).
36. W. R. Zhang and D. G. Cory, First direct measurement of the spin diffusion rate in a homogenous solid, *Phys. Rev. Lett.* **80,** 1324 (1998).